Fourier and Likelihood Analysis in NMR Spectroscopy

By

David R. Brillinger
Department of Statistics
University of California
Berkeley, California 94720

and

Reinhold Kaiser
Department of Physics
University of New Brunswick
Fredericton, Canada E3B 5A3

Technical Report No. 287
January 1991

$2\pi \neq 1$

Department of Statistics
University of California
Berkeley, California 94720

$2\pi \neq 1$

$2\pi \neq 1$

FOURIER AND LIKELIHOOD ANALYSIS IN NMR SPECTROSCOPY

DAVID R. BRILLINGER† AND REINHOLD KAISER‡

Abstract. Nuclear magnetic resonance (nmr) is a quantum mechanical phenomenon that may be employed to study the structure of a variety of molecules, crystals and polymers. The time series data collected are traditionally Fourier transformed and the Fourier amplitudes examined for peaks. Higher-order transforms are sometimes employed. If the substance and relevant interactions are known one can set down a set of differential equations describing the temporal evolution of the state matrix that describes the system. These differential equations are bilinear in the input and the system state. The time series recorded in an experiment is, up to noise, a linear function of the entries of the state matrix. In the research to be presented, the Fourier techniques of analysis are compared with a maximum likelihood analysis based on the state matrix. Results are presented for an experiment involving 2,3-dibromothiophene.

Key words. bilinear system, Bloch equations, Fourier analysis, maximum likelihood estimation, m-sequence, residual analysis, signal-generated noise, system identification, transfer function

AMS(MOS) subject classifications. 62M15, 62P99

1. Introduction. The concerns of this paper are to provide an example of the maximum likelihood analysis of data collected in nuclear magnetic resonance (nmr) spectroscopy and to give some comparative discussion of maximum likelihood and Fourier based techniques. The nmr case is based upon revered theory allowing con-

---

† Department of Statistics, University of California, Berkeley. Research supported by NSF Grant DMS-8900613.

‡ Department of Physics, University of New Brunswick, Fredericton, Canada E3B 5A3. Research supported by NSERC Grant A1565.

ceptual modelling and a state space formulation. The layout of the paper is: first some pertinent background concerning nmr is set down, next comes some formal development following the basic theoretical layout, then a discussion of the problem as one of system identification is presented. Sections 5 and 6 describe a particular laboratory experiment carried out and present an analysis of its results. The paper concludes with a discussion comparing and contrasting the various approaches and mentions some possible future work.

2. Nuclear magnetic resonance spectroscopy. Nuclear magnetic resonance spectroscopy is a quantum mechanical phenomenon that may be employed to study the structure of a variety of molecules, crystals and polymers. In the procedure, a sample of the material whose structure is to be investigated is placed in a strong magnetic field, 1.41 Tesla for our measurements. This field is constant in time and uniform in space throughout the volume occupied by the sample. It exerts a mechanical torque on those nuclei in the sample that carry a magnetic dipole moment, tending to align these nuclei in the direction of the field. However, the magnetic dipole of a nucleus is associated with an intrinsic spin angular momentum, and the torque consequently causes a gyroscopic precession of the nuclear spin axis about the direction of the magnetic field. The precession frequency is proportional to the magnetic field strength at the site of a nucleus and thus provides information about the nuclear environment. The nuclear precessional motion may be stimulated by applying to the sample a weak oscillating magnetic field directed at right angles to the strong constant magnetic field. A resonance effect occurs when the oscillation frequency of this weak field coincides with a nuclear precession frequency. The nuclear motion is sensed by monitoring the voltage that is induced by the moving nuclear magnetic dipoles in a coil that is wound at right angles to the strong magnetic field. An nmr spectrum for a particular sample is a graph showing the amplitude of this induced voltage as function of the oscillation frequency of the weak stimulating magnetic field.

The data used for our work are derived from a sample of 2,3-dibromothiophene. This substance is liquid at room temperature, its molecules have the chemical structure shown in Figure 1. The naturally abundant isotopes of carbon (^{12}C) and sulfur (^{32}S) have zero magnetic dipole moment and are thus not observable by nmr methods. The stable bromine isotopes (^{79}Br) and (^{81}Br) both carry magnetic dipole moments, but they also carry a sizeable electric quadrupole moment which couples them to fluctuating electric fields in the sample and this also makes them inactive for our work. Our data thus arise from the magnetic resonances of the nuclei (protons) of the two hydrogen atoms labelled H_A and H_B in Figure 1. The nuclei are surrounded by molecular electrons that hold the atoms in the structure of Figure 1. These electrons tend to shield the nuclei from the strong applied field. The proximity of the sulfur atom causes the electronic shielding of nucleus H_A to differ slightly from the shielding available to H_B, thus leading to slightly different precession frequencies for H_A and H_B. In more detail, the precession frequency of hydrogen nuclei in our 1.41 Tesla field is 6.00E7 Hz, and the difference of resonance frequencies of H_A and H_B was found as 32.57 Hz, so the nmr "chemical shift" between H_A and H_B amounts to 32.57/6.00E7 = 0.543 parts per million (ppm).

The nmr spectrum of 2,3-dibromothiophene is shown in Figure 3b below. The two doublets of resonance peaks are here separated by the 32.57 Hz chemical shift and each doublet arises from one hydrogen nucleus H_A or H_B, respectively. The doublet splitting of the resonances is caused by a coupling of H_A with H_B via the magnetic field set up at H_B by the magnetic moment of H_A, and vice versa. (More precisely, it is the part of this coupling that is not averaged to zero by the thermal tumbling of the molecule in the liquid.) Quantum mechanics yields for each hydrogen nucleus in a strong magnetic field, two stationary states with nuclear spin axis either parallel or antiparallel to the direction of the magnetic field. So, one H_B resonance peak arises from molecules having the H_A spin axis parallel to the magnetic field, the other from molecules having the H_A spin axis antiparallel to the field. The strength of this intramolecular nuclear coupling is measured by the doublet splitting as J=5.76 Hz for the case of Figure 3.

Other significant parameters are various relaxation times classified as either longitudinal T_1 or transverse T_2. The longitudinal T_1 is the time constant with which the nuclear magnetization eventually aligns itself with the direction of the strong magnetic field after the sample is placed into the magnet. The transverse T_2 are the time constants governing the "frictional damping" of the oscillatory components of the state vector that describe the nuclear precession. These relaxation times depend on thermal random motions in the sample, they are of several seconds duration for our sample.

A quantitative description of the nuclear magnetic spin dynamics in a macroscopic sample requires a quantum mechanical formulation in terms of the spin density operator ρ, see Slichter (1990) and Ernst *et al.* (1987). The motion of this operator is described by the von Neumann equation

$$\text{(2.1)} \qquad \frac{d\rho}{dt} = \mathbf{R}(\rho-\rho^T) + (\mathbf{H}\rho-\rho\mathbf{H})/i\hbar$$

Here, **R** is a superoperator describing relaxation of the density operator towards its thermal equilibrium value ρ^T, the symbol $\hbar$ designates Planck's constant/2π, and $i = \sqrt{-1}$. The symbol **H** designates the Hamilton operator for the energy of the nuclear magnetic dipoles in the magnetic fields that are applied to the sample. It can be separated into two parts,

$$\text{(2.2)} \qquad \mathbf{H} = \mathbf{H}_0 + \mathbf{H}_1(t)$$

such that $\mathbf{H}_0$ describes the interactions of the nuclei with the strong magnetic field and the intramolecular coupling, and $\mathbf{H}_1$ describes the interaction with the oscillating magnetic field that is used to stimulate the precession motion. The first term, $\mathbf{H}_0$, is constant in time and strong compared to the second term, $\mathbf{H}_1(t)$, which is proportional to the stimulating field.

The operators in (2.1) are linear and it is convenient to represent them by matrices operating in the space spanned by the eigenvectors of $\mathbf{H}_0$. For our sample which contains only two nmr active hydrogen nuclei, this space is of dimension 4. Furthermore, it is numerically helpful to freeze the fast precession by transforming to a physical x,y,z-space that rotates about the z direction of the strong magnetic field at 6E7 revolutions/sec. Equations (2.1) then take the form shown in Figure 2 for the 16 entries ρ_{jk} representing the density operator ρ in matrix form. Only ten equations are written out in Figure 2, the remaining six are complex conjugate of the last six since ρ is hermitian. The relaxation operator **R** has been represented by relaxation times T.

The four diagonal elements ρ_{jj} may be interpreted as probabilities normalized by $Tr(\rho) = 1$, to have the spin system in each of the four eigenstates of the Hamiltonian $\mathbf{H}_0$. Without stimulus and in thermal equilibrium, these are the only nonzero elements with values

$$(2.3) \qquad \rho_{11}^T = (1+\varepsilon)/4 \qquad \rho_{22}^T = \rho_{33}^T = 1/4 \qquad \rho_{44}^T = (1-\varepsilon)/4$$

with $\varepsilon \ll 1$ depending on sample temperature and magnetic field strength. The off-diagonal elements describe the precessional motion and may be interpreted as coherences between eigenstates of $\mathbf{H}_0$. The stimulus $X(t)$ links them to the diagonal elements since $\mathbf{H}_1$ does not commute with $\mathbf{H}_0$. They may be classified by the quantum jump involved in the coherence as follows. The set $\rho_{12}, \rho_{13}, \rho_{24}, \rho_{34}$ is responsible for the output signal induced by the precessing nuclear magnetic moments in the receiver coil. Depending on whether this coil is wound around the sample in the x or y direction, the output is

$$(2.4) \qquad \begin{aligned} Y_x &= (c+s)\mathrm{Re}(\rho_{12}+\rho_{24}) + (c-s)\mathrm{Re}(\rho_{13}+\rho_{34}) \\ Y_y &= (c+s)\mathrm{Im}(\rho_{12}+\rho_{24}) + (c-s)\mathrm{Im}(\rho_{13}+\rho_{34}) \end{aligned}$$

Here and in Figure 2 the meaning of symbols is:

J is the coupling strength of H_A with H_B.

ω_A, ω_B are the precession frequencies in the rotating coordinate frame of H_A and H_B, respectively

$$\delta = |\omega_A - \omega_B| = \text{chemical shift}$$

$$\theta = arctan\,(J/\delta) \qquad c = \cos(\theta/2) \qquad s = \sin(\theta/2) \qquad \sqrt{\ } = \sqrt{J^2+\delta^2}$$

γ is a scale factor for the input amplitude

The equations of Figure 2 show that, in the absence of a stimulus X, the four elements ρ_{12}, ρ_{13}, ρ_{24}, ρ_{34} precess in the rotating coordinate frame like $\exp\{-1/T_2+i\,\omega\}$ with frequencies

$$\omega = (\pm J \pm\sqrt{J^2 + (\omega_A - \omega_B)^2})/2 + (\omega_A + \omega_B)/2 \tag{2.5}$$

These are the four nmr resonance frequencies. The superposition of the four damped oscillations that are observed in some simulated output $Y(t)$, t, $=0,\dots,T-1$, in response to an impulse stimulus, are shown in Figure 3a below. The corresponding Fourier spectrum

$$\left|\sum_{t=0}^{T-1} Y(t) e^{-i\lambda t}\right| \tag{2.6}$$

is shown in Figure 3b. These four ρ elements are referred to as single quantum coherences because they are associated with emission or absorption by a molecule of a single quantum $\hbar$ of angular momentum. Of the remaining off-diagonal elements, ρ_{23} is a zero quantum coherence and ρ_{14} is a double quantum coherence. They are not directly observable in the output Y.

The 16 equations of motion for the ρ_{jk} may be written in vector form as

$$\frac{d\mathbf{S}(t)}{dt} = \mathbf{a} + \mathbf{A}\mathbf{S}(t) + \mathbf{B}\mathbf{S}(t)X(t) \tag{2.7}$$

with $\mathbf{S}$ a 16-vector containing the ρ_{jk}, $\mathbf{a}$ a 16-vector holding the four ρ_{jj}^T/T_1 thermal equilibrium terms and zero otherwise, $\mathbf{A}$ a 16x16 matrix collecting the diagonal terms of Figure 2, and $\mathbf{B}$ a 16x16 matrix holding the off-diagonal terms. $\mathbf{B}$ is symmetric with entries purely imaginary, it does not commute with $\mathbf{A}$. The output equations (2.4) may be written

$$Y(t) = \mathrm{Re}(\mathbf{c}^{\tau}\mathbf{S}(t)) \tag{2.8}$$

with suitable 16-vectors **c**.

3. A problem of system identification. The transition equation (2.7) and the measurement equation (2.8) together describe a system carrying input signals, X, over into corresponding output signals, Y. The concern is to determine the unknown parameters of the system. A variety of techniques have been proposed. In the previous section it was seen how Fourier transforming the response to a pulse could lead to estimates of the "frequency" parameters, and indeed this technique has long been employed in nmr spectroscopy, see eg. Becker and Farrar (1972). Information can also be gained via a succession of two-pulse experiments and those experiments had the possibility of displaying the presence of cross-coupling of frequencies for "large" input, X. The practice of nmr spectroscopy has moved on to the employment of multipulse sequences, eg. Kay. *et al.* (1990) where sequences of 10 pulses are employed.

In the case of step-funtion input, one can set down explicit representations for the solutions of (2.7) , see for example Brillinger (1985, 1990). Suppose, now, that

$$\begin{aligned} X(t) &= 0 \quad \text{for } s \le t < u \\ X(t) &= x \quad \text{for } u \le t < v \\ X(t) &= 0 \quad \text{for } v \le t \end{aligned} \tag{3.1}$$

This is a pulse of height x and width $v-u$. Writing $\mathbf{D} = \mathbf{A} + \mathbf{B}x$, the solution to (2.6) is given by

$$\begin{aligned} \mathbf{S}(t) &= e^{\mathbf{A}(t-s)}\mathbf{S}(s) + \mathbf{A}^{-1}[e^{\mathbf{A}(t-s)}-\mathbf{I}]\mathbf{a} \quad \text{for } s \le t < u \\ \mathbf{S}(t) &= e^{\mathbf{D}(t-u)}\mathbf{S}(u)+\mathbf{D}^{-1}[e^{\mathbf{D}(t-u)}-\mathbf{I}]\mathbf{a} \quad \text{for } u \le t < v \\ \mathbf{S}(t) &= e^{\mathbf{A}(t-v)}\mathbf{S}(v) + \mathbf{A}^{-1}[e^{\mathbf{A}(t-v)}-\mathbf{I}]\mathbf{a} \quad \text{for } v \le t \end{aligned} \tag{3.2}$$

referrring respectively, to the periods before, during and after the pulse.

Figure 3a gives an example of the response, Y, to a pulse (3.1) applied to the system in thermal equilibrium, employing parameter values appropriate to a 2,3-DBT sample, see Appendix A.1. 600 points have been plotted. The bottom graph gives the modulus of the Fourier transform of this output as computed by (2.6). Four substantial peaks are seen to be present in the latter. This could have been anticipated from the form of the matrix **A** and expression (3.2). The frequencies are those of (2.5).

Figure 4 gives the evolution of the nondiagonal entries of the state matrix following the pulse input. The series fluctuates with the frequencies of the elements of **A**. The variates ρ_{23} and ρ_{14} remain 0. An interesting phenomenon is present in the plots of the second and fifth rows. There seem to be beats, suggesting the presence of two frequencies. To better understand this phenomenon, Figure 5 provides a graph of 50 points from the function

$$e^{-\alpha t}\sin(\beta t)$$

with parameter values corresponding to those of the numerical experiment. The phenomenon is now seen to arise from the particular relationship of the sampling rate and the base frequency. Typically but 1 or 2 points are being plotted between the zero crossings and hence the deceptive appearance.

Next suppose a pulse further to (3.1) is input to the system commencing at time u_1. Suppose it is has amplitude x_1 and width v_1-u_1, then the equations of subsequent evolution are

$$\mathbf{S}(t) = \exp\{\mathbf{D}_1(t-u_1)\}\mathbf{S}(u_1) + \mathbf{D}_1^{-1}[\exp\{\mathbf{D}_1(t-u_1)\}-\mathbf{I}]\mathbf{a} \qquad \text{for } u_1<t\leq v_1$$

$$(3.3) \qquad \mathbf{S}(t) = \exp\{\mathbf{A}(t-v_1)\}\mathbf{S}(v_1) + \mathbf{A}^{-1}[\exp\{\mathbf{A}(t-v_1)-\mathbf{I}]\mathbf{a} \qquad \text{for } v_1<t$$

Here $\mathbf{D}_1 = \mathbf{A}+\mathbf{B}x_1$.

If $|\gamma x|$ is small, then the system is approximately linear and the output, Y, will show simply the frequencies of ρ_{12}, ρ_{24}, ρ_{13}, ρ_{34} following Figure 2. If $|\gamma x|$ is large, nonlinear phenomena may show themselves. To illustrate this, let $\Delta(t)$ denote a pulse starting at time 0 having width σ. Consider a suite of two-pulse experiments with input $X(t) = \Delta(t)+\Delta(t-s)$, for a succession of values s. That, for example, the frequency of ρ_{12} interacts with that of ρ_{14}, may be seen from the fifth equation of Figure 2.

Simulations of this technique were carried out. Figure 6 presents the absolute value of the two dimensional Fourier transform of the outputs, Fourier transforming with respect to s, the interval between pulses and u, time since the second pulse finished. In the case of small input, (1 degree flip angle, see Appendix A.1 for definition), there are only off-axis peaks apparent along the diagonal $\lambda = \mu$. For large input, (90 degree flip angle), a host of off-diagonal peaks appear. The peaks along the horizontal axis occur in the manner of expression (4.9) below.

4. System identification by cross-correlation. Nmr spectroscopy has on occasion employed stochastic or pseudo-stochastic input, see eg. Ernst (1970), Kaiser (1970), Blümich (1985). One cross-correlates the input and output and then Fourier transforms the result. This may be motivated as follows: successive substitutions into the equation (2.7), assuming **B** or X small, leads to

$$(4.1)\ \mathbf{S}(t) = -\mathbf{A}^{-1}\mathbf{a} + \int^{t} e^{\mathbf{A}(t-s)}\mathbf{C}X(s)ds + \int^{t}\int^{s} e^{\mathbf{A}(t-s)}\mathbf{B}e^{\mathbf{A}(s-r)}\mathbf{C}X(r)X(s)drds + \cdots$$

with $\mathbf{C} = -\mathbf{B}\mathbf{A}^{-1}\mathbf{a}$, see eg, Blümich and Ziessow (1983), Banks (1988), Brillinger (1990). The linear, quadratic and third-order *asymmetric* (or triangular) transfer functions here are

$$(4.2)\qquad (i\lambda\mathbf{I} - \mathbf{A})^{-1}\mathbf{C}$$

$$(4.3)\qquad (i(\lambda+\mu)\mathbf{I} - \mathbf{A})^{-1}\mathbf{B}(i\lambda\mathbf{I} - \mathbf{A})^{-1}\mathbf{C}$$

$$(4.4)\qquad (i(\lambda+\mu+\nu)\mathbf{I} - \mathbf{A})^{-1}\mathbf{B}(i(\lambda+\mu)\mathbf{I} - \mathbf{A})^{-1}\mathbf{B}(i\lambda\mathbf{I} - \mathbf{A})^{-1}\mathbf{C}$$

with similar expressions for the higher-order cases. It is to be noted that peaks will occur in the absolute values of the linear transfer function at the resonance frequencies indicated earlier. For the quadratic and higher-order terms, a matching of frequencies connected by **B** is needed. Workers in nmr spectroscopy speak of "coupling" in this type of circumstance.

In the kernel approach to nonlinear systems analysis, it is usual to employ *symmetric* transfer functions in expansions such as (4.1), writing for example

(4.5)
$$\mathbf{S}(t) \approx \int \mathbf{a}_1(u)X(t-u)du + \iint \mathbf{a}_2(u,v)X(t-u)X(t-v)dudv + \iiint \mathbf{a}_3(u,v,w)X(t-u)X(t-v)X(t-w)dudvdw$$

with $\mathbf{a}_2$ and $\mathbf{a}_3$ symmetric in their arguments. In the case that stationary Gaussian input has been employed and the system is quadratic, (i.e. $\mathbf{a}_3 = 0$ in (4.5)), the linear transfer function is given by

(4.6)
$$\mathbf{A}_1(\lambda) = \mathbf{f}_{SX}(\lambda)/f_{XX}(\lambda)$$

while the quadratic one is given by

(4.7)
$$\mathbf{A}_2(-\lambda,-\mu) = \mathbf{f}_{XXS}(\lambda,\mu)/2f_{XX}(\lambda)f_{XX}(\mu)$$

with f_{XX} the input power spectrum, with $\mathbf{f}_{SX}$ the cross-spectrum of the input and output and with $\mathbf{f}_{XXS}$ a cross-bispectrum of the input and output, see eg. Tick (1961). These equations suggest how to estimate $\mathbf{A}_1$ and $\mathbf{A}_2$. Extensions exist to the higher-order terms, see Wiener (1958), Brillinger (1970), Marmarelis and Marmarelis (1978), Blümich (1985). In the case of pseudorandom input, expressions (4.6) and (4.7) hold approximately, see eg. Marmarelis and Marmarelis (1978).

The following hybrid technique shows how elementary cross-correlation techniques may be used to display the presence of cross-coupling. Suppose N denotes a white noise sequence with variance σ^2. Consider the suite of experiments in which the input is taken to be $N(t) + N(t-s)$ for a succession of values s. (Such an experiment was discussed in Blümich (1981).) For each individual experiment estimate the cross-spectrum, $\mathbf{f}_{SN}(\lambda,s)$. Next Fourier transform this with respect to s to obtain a function of two frequencies. Off-diagonal peaks will be indicative of the presence of cross-coupling. To be specific, suppose that $\mathbf{S}(t)$ is given by (4.5) and that N is white noise with third cumulant $\kappa_3 = 0$ and fourth κ_4. By elementary computations (see Appendix B) one can show that for given lag s, $\mathbf{f}_{SN}(\lambda,s)$ is given by

(4.8)
$$\frac{\sigma^2}{2\pi}(1 + e^{-i\lambda s})\mathbf{A}_1(\lambda) + \left[\frac{\sigma^2}{2\pi}\right]^2 (1 + e^{-i\lambda s})3\int \mathbf{A}_3(\lambda,\nu,-\nu)\,|\,1 + e^{-i\nu s}\,|^2 d\nu$$

plus a term in κ_4. Here $\mathbf{A}_3$ is assumed symmetric in its arguments. (It will be obtained by permuting the arguments of (4.4) and averaging.) Taking the Fourier transform of (4.8) with respect to s and denoting the corresponding argument by μ, leads to

$$\text{(4.9)}\qquad \sigma^2\mathbf{A}_1(\lambda)[\delta(\mu)+\delta(\mu+\lambda)] + \frac{\sigma^4}{\pi}3\int\mathbf{A}_3(\lambda,\nu,-\nu)d\nu[\delta(\mu)+\delta(\mu+\lambda)]$$
$$+\frac{\sigma^4}{\pi}3[\mathbf{A}_3(\lambda,\mu,-\mu)+\mathbf{A}_3(\lambda,\mu+\lambda,-\mu-\lambda)]$$

plus a term in κ_4 and with δ the Dirac delta function. The delta functions are seen to lead to ridges about the lines $\mu = 0$ and $\mu = -\lambda$. Focusing on the last term of (4.9) and following expression (4.4) the terms

$$\text{(4.10)}\qquad (i\lambda\mathbf{I}-\mathbf{A})^{-1}\mathbf{B}(i(\lambda+\mu)\mathbf{I}-\mathbf{A})^{-1}\mathbf{B}(i\lambda\mathbf{I}-\mathbf{A})^{-1}\mathbf{C}$$

and their permuted variants will appear. The matrix $\mathbf{A}$ is diagonal hence peaks will appear at appropriate locations (λ,μ).

A numerical simulation experiment was carried out to examine the above technique. The noise process N consisted of pulses of amplitudes ±1 the values being independent and equiprobable. The flip angle was 10 degrees and otherwise the parameters were as in Appendix A.1. Figure 7 presents the results of the analysis. Figure 7a provides the absolute value of $\mathbf{c}^\tau$(4.10) supplemented by the 5 other permuted terms. A variety of peaks and cross-peaks are seen to appear. Figure 7b is the result of estimating (4.9). Peaks and cross-peaks occur as well as indications of the presence of the delta functions. The procedure does appear practical. In the estimation the s values ran from 1 to 128 and the cross-spectrum was estimated at 128 frequencies by averaging cross-periodograms of 100 successive stretches of data.

There are contrasting circumstances for employing pulse input and "noise" input. The noise input has the advantage that input power required is low (but applied over a longer time). It has the further advantage that the response need be measured only once and thereafter can be subjected to a number of modelling analyses. The pulse input requires a high power and in consequence can be hard to produce and even damaging. However the approach is flexible, with specific pulse sequences able to be tailored to specific purposes.

Next consideration turns to data collected in a laboratory experiment.

5. Experimental details. The equations shown in Figure 2 describe the dynamics of the nuclear spin system in a x,y,z coordinate system that rotates at 6E7 rev/sec about the z direction of the strong magnetic field. The nmr spectrometer is fixed in the laboratory, and the rotation is simulated electronically by providing interaction with the sample via a 60 MHz radio frequency (rf) carrier sinusoid. This carrier is generated by multiplying with 6 the frequency of the output sinusoid of a 10 MHz quartz crystal oscillator that serves as master clock for the spectrometer. The input stimulus X modulates this carrier by means of a balanced modulator, and the nuclear output voltage Y is demodulated in a phase sensitive detector which is referenced to the carrier sinusoid. The phase angle of this reference depends on cable lengths, time delays in electronic components, etc, and the measured output is thus a projection in some direction ϕ in the x,y plane of the rotating coordinate frame,

$$Y(t) = \cos\phi \, Y_x(t) + \sin\phi \, Y_y(t) + noise \tag{5.1}$$

This output of the phase sensitive detector is low-pass filtered by passing it through a 4-pole Bessel filter set to a 150 Hz corner frequency in order to reduce high frequency noise that would be folded into the Nyquist bandwidth by the sampling described below. The level of the input stimulus exceeds the nuclear response signal by some 100 dB, and to avoid direct crosstalk from the input to the output, the modulated carrier is gated to produce short rf pulses, and the detector output is sampled between input pulses. This time sharing system is governed by a digital pulse generator that is driven from the 10 MHz spectrometer clock. The data studied were generated by deriving the input stimulus from a 12-stage binary shift register with feedback such as to produce the m-sequence

$$x_j = x_{j-1}x_{j-4}x_{j-6}x_{j-12} \tag{5.2}$$

starting from $x_j = -1$ for $j = 1,2,...12$. The balanced modulator converts the +1,-1 levels of the shift register to 0 degree, 180 degree phase shifts of the 60 MHz carrier. The shift register was driven from the pulse generator at a rate to produce 150 bits/sec. The advantage of employing an m-sequence is that input data need not be recorded. The m-sequence has period 4095 bits corresponding to 27.3 seconds, and received data were recorded for one such period after the nuclear spin system had run through at least one prior period to reach a steady state. The pulse generator was programmed to use the dwell time of each bit, 1/150 sec = 6667 μsec, for the time sharing of input and output as follows.

Time 0 : open rf gate for 30 μsec to apply input pulse to nuclear sample;
77 μsec: shift m-sequence to next bit;
3567 μsec: sample output of antialiasing filter;
6667 μsec: loop back to time 0.

The gated and modulated rf carrier was amplified such that a 30 μsec pulse produced a 3.6 degree flip angle, (see Appendix A.1 for the definition). It was later learned that the 150 Hz antialiasing filter causes a time delay of 1/300 sec so that the nuclear output was actually sampled 204 μsec after the end of the input pulse. However, crosstalk was still suppressed.

The 150 Hz sampling rate of the output corresponds to a Nyquist frequency window from 0 to 75 Hz, and the precession frequencies of the hydrogen nuclei must be within this window in the rotating coordinate frame, i.e. within ($6E7$ ±75)Hz in the fixed laboratory frame. Since this frequency is proportional to the intensity of the strong magnetic field, the 1.41 Tesla electromagnet must be controlled to considerably better than 1 part per million. To this end, our sample held a homogeneous mixture of 0.24 ml 2,3-dibromothiophene with 0.18 ml dimethylsulfoxide-d6. The latter compound has six nmr-active deuterium nuclei per molecule, and these yield a single nmr resonance near 9.21 MHz in a 1.41 Tesla field. A second spectrometer was set up to operate with the same probe using a rf carrier derived from the 10 MHz system clock by means of a frequency synthesizer such as to be adjustable near 9.21 MHz. The output of this second spectrometer is used in a feedback loop to hold the strong magnetic field on the peak of the deuterium resonance of the sample.

6. RESULTS.

6.1. Fourier analysis. The top graph of Figure 8 displays the stretch of output corresponding to the first 600 points of the m-sequence input. The bottom graph gives an estimate of $|\mathbf{c}^\tau \mathbf{A}_1(\lambda)|$ as computed in the manner of expression (4.6). The second-order spectra that appear were estimated by structuring the data into 15 segments of 512 successive points, the segments were overlapped by 256 points. Prior to the Fourier transform, the values were tapered. The cross- and ordinary periodograms were computed for each segment, and these then averaged to obtain estimates of f_{YX} and f_{XX}, and thereby an estimate of $|\mathbf{c}^\tau \mathbf{A}_1|$. This graph displays four substantial peaks, in the manner of Figure 3. From the locations of these peaks the parameters ω_A, ω_B, J may be estimated by inspection.

6.2. Maximum likelihood analysis. In practice the electronics of the measurement process lead to a measurement equation more complicated than (2.8). A further parameter needs to be introduced. It is an unknown, but small, time delay, τ, relative to the input pulse timing at which the sampled values are recorded. The output is still given by (5.1) but with τ built into Y_x and Y_y. For given initial values, $\mathbf{S}(0)$, for the state vector and given parameter values, the signal $\mathbf{S}(t)$ may be evaluated recursively following expressions (3.2) and (3.3). If the noise in (5.1) is Gaussian white, then one has a nonlinear regression problem and is lead to estimate the unknowns by minimizing

$$\sum_{j=1}^{n} |Y(j) - \beta[\cos\phi\, Y_x(j) + \sin\phi\, Y_y(j)]|^2 \tag{6.1}$$

with j indexing the times of measurements and with β a further parameter introduced to handle the unknown scaling of the measurement process. Appendix A.2 presents some further computational details.

6.3 Results of the analyses. In the results to be presented, the thermal equilibrium values were taken to be (2.3). Here ε is a small positive quantity, that is effectively a scaling variable. Maximum likelihood fitting was carried out for the full set of 4095 data points and separately for four successive stretches of 1000 points. The unknown parameters estimated were: J, ω_A, ω_B, T_1, T_2, ϕ, τ, β and the unknown $\rho_{jk}(0)$, in total 24 unknowns. Figure 9 and Figures 10, 11, 12, 13 provide the results. The first panel, in each case is a scatter plot of the fitted versus the corresponding observed values. The second and third panels are respectively plots of the logarithms of the absolute values of the Fourier transforms of the residual and observed series. The final panel is a scatter plot of the two log |FT|'s versus each other.

The complete data set analysis, displayed in Figure 9, resulted in a correlation of .81 between fitted and observed data values. The second through fourth panels in this Figure suggest the presence of signal-generated noise. Specifically note the parallel shapes in the second and third and the scatter parallel to the diagonal line in the fourth panel. It is interesting to note how the peak just above 60 Hz. in the third panel has emerged from the "noise" level.

The results are similar, see Figures 10, 11, 12, 13, for the separate stretches of 1000 except that the correlation coefficients are considerably higher, .93, .90, .96, .96. For the fourth stretch it is notable how the "birdie" near 60 Hz. has emerged from the noise. The following table presents the estimates for the principal parameters. The relaxation times were poorly determined.

	J	ω_A	ω_B	$\omega_A - \omega_B$
1-4095	5.728	49.718	17.154	32.564
1-1000	5.714	49.465	16.830	32.635
1001-2000	5.848	49.784	17.323	32.461
2001-3000	5.742	49.795	17.233	32.562
3001-4000	5.733	49.661	17.028	32.633

7. Discussion. Three techniques for estimating the parameters of nmr spectroscopy will now be discussed. The first technique is to compute spectra of some order following pulse or noise input. The second is to fit sums of exponential cosines following pulse input. The third is to build a conceptual model and employ maximum likelihood. This last was the special concern of this paper. Each technique has advantages and disadvantages.

Advantages of the Fourier-based techniques are that they are direct, robust and do not need full models. Disadvantages are that some parameters cannot be estimated and rephasing may be needed to reduce leakage between frequencies.

An advantage of the exponential-sinusoid model, as implemented in Miller and Greene (1989) for example, is that a full model is not needed. However pulse input is needed and some parameters cannot be estimated.

Advantages of the full modelling approach include: the parameters are interpretable, efficient fitting methods are available with corresponding estimates of uncertainty, there is flexibility in parametrization, the state variables may be estimated and tracked, coupling/phasing/nonlinearities are handled as a matter of course. An advatage of ±1 input is that only 3 matrix exponentials need be computed. Disadvantages are that: a full model is needed and this will be difficult for large molecules, which parameters can be effectively estimated and when remains to be understood, initial values are needed for the optimization routines.

A hybrid approach in which a simple model is fit and then the residuals are examined by Fourier techniques for peaks would seem likely to be effective in a variety of circumstances.

8. Future work. The source of the signal-generated noise remains a mystery. There are several ways to approach the problem. One is to better model the anti-aliasing filter. A second is to sample the output values more often. A third is to seek other electronic noise sources. If these approaches are unsuccessful then the least squares criterion (6.1) would be replaced by one from generalized least squares incorporating the apparent noise spectrum form.

In future work standard errors will be provided for the estimates.

9. Acknowledgement. We would like to thank Reuben Hale for a helpful conversation concerning the "beating" in Figure 4.

REFERENCES

[1] S. P. BANKS, Mathematical Theories of Nonlinear Systems, Prentice Hall, London, 1988.

[2] E. D. BECKER AND T. C. FARRAR, Fourier transform spectroscopy, Science, 178 (1972), pp.351-368.

[3] B. BLUMICH, Nichtlineare Rauschanalyse in der magnetischen Kernresonanzspektroskopie, Dissertation, TU Berlin (1981).

[4] B. BLUMICH, Multidimensional spectroscopy II. Analysis of 3D lineshapes obtained from stochastic N.M.R. of two level systems, Molecular Physics, 48 (1983), pp. 969-980.

[5] B. BLUMICH, Stochastic nmr spectroscopy, Bull. Magnet. Resonance, 7 (1985), pp. 5-26.

[6] B. BLUMICH AND D. ZIESSOW, Nonlinear noise analysis in nuclear magnetic resonance spectroscopy. 1D, 2D, and 3D spectra. J. Chem. Phys. 78 (1983), pp. 1059-1076.

[7] D. R. BRILLINGER, The identification of polynomial systems by means of higher

order spectra, J. Sound Vib. 12 (1970), pp. 301-313.

[8] D. R. BRILLINGER, Some statistical aspects of nmr spectroscopy, Actas del Segundo Congresso Latinoamericano de Probabilidad y Estatistica Matematica, Caracas (1985), pp. 9-17.

[9] D. R. BRILLINGER, A study of second- and third-order spectral procedures and maximum likelihood in the identification of a bilinear system. IEEE Trans ASSP, 38 (1990), pp. 1238-1245.

[10] R. E. ERNST, Magnetic resonance with stochastic excitation, J. Magnetic Resonance, 3 (1970), pp. 10-27.

[11] R. E. ERNST, G. BODENHAUSEN AND A. WOKAUN, Principles of Nuclear Magnetic Resinance in One and Two Dimensions, Clarendon press, Oxford (1987).

[12] R. KAISER, Coherent spectrometry with noise signals, J. Magnetic Resonance, 3 (1970), pp. 28-43.

[13] L. E. KAY et al., Four dimensional heteronuclear triple-resonance nmr spectroscopy of interleukin-1β in solution, Science, 249 (1990), pp. 411-414.

[14] P. MARMARELIS AND V. Z. MARMARELIS, Analysis of Physiological Systems: the White Noise Approach, Plenum Press, New York, 1978.

[15] M. I. MILLER and A. S. GREENE, Maximum-likelihood estimation for nuclear magnetic resonance spectroscopy, J. Magnetic Resonance 83 (1989), pp. 525-548.

[16] C. MOLER AND C. VAN LOAN, Nineteen dubious ways to compute the exponential of a matrix, SIAM Review, 20 (1978), pp. 801-836.

[17] C. P. SLICHTER, Principles of Magnetic Resonance, Springer Verlag, Berlin 3rd edition (1990).

[18] L. J. TICK, The estimation of transfer functions of quadratic systems, Technometrics, 3 (1961), pp. 563-567.

[19] N. WIENER, Nonlinear Problems in Random Theory, MIT Press, Cambridge, 1958.

APPENDIX

A.1 Simulation Details. For the simulations described in Sections 3 and 4, the following parameter values were employed: $\omega_A = 49.8\ Hz$, $\omega_B = 17.2\ Hz$, $J = 5.77\ Hz$, $T_1 = 4.0$ seconds and all the other $T's$ 2.0 seconds The diagonal elements of $\rho(0)$ were $(1+\varepsilon)/4$, 1/4, 1/4, $(1-\varepsilon)/4$ respectively with $\varepsilon = .01$ and the off diagonals were all 0. , the spacing between samples was 1/150 seconds, the pulse width was taken to be 30/6667 of the sampling interval, with the pulses applied 3100/6667 of the sampling interval after a measurement. These values were meant to mimic the laboratory experiment.

The amplitude of the applied stimulus is typically described in terms of a *flip angle*. In the case of a pulse of width σ time units and amplitude γx the flip angle is given by $\gamma x \sigma$

A.2 Computational Details. A few computational aspects of the study will be mentioned. The computations were via FORTRAN complex double precision on Sun and Sparc workstations. In order to generate the signal, matrix exponentials are needed. Computing such things is not elementary, see eg. Moler and Van Loan (1978). The procedure adopted in the present work was to first obtain the decomposition, $\mathbf{A} = \mathbf{U}\Lambda\mathbf{U}^{-1}$, via a NAG routine and from that obtain the matrix exponential, $\exp\{\mathbf{A}\} = \mathbf{U}\exp\{\Lambda\}\mathbf{U}^{-1}$. The Harwell routine VA09A was employed to minimize the sum of squares in the parameters appearing in nonlinear fashion. The initial state parameter, S(0), appears in a linear fashion, so in the minimization it was first "determined" for given values of the other parameters, then these parameters were determined in turn. Iteration was continued until apparent convergence. Several positive parameters were expressed as exponentials to stabilize the computations.

B. The Derivation of (4.8) and (4.9). It is convenient to approach the problem via the Cramér representation

$$N(t) = \int e^{it\lambda} dZ_N(\lambda)$$
$$\mathbf{S}(t) = \int e^{it\lambda} d\mathbf{Z}_{\mathbf{S}}(\lambda)$$

where

$$cov\,\{dZ_N(\lambda), dZ_N(\mu)\} = \delta(\lambda-\mu) f_{NN}(\lambda) d\lambda d\mu$$
$$cov\,\{dZ_{\mathbf{S}}(\lambda), dZ_N(\mu)\} = \delta(\lambda-\mu) \mathbf{f}_{SN}(\lambda) d\lambda d\mu$$

Here $cov\,\{X, Y\} = E\{X\overline{Y}\}$ for zero mean complex variables and $f_{NN} = \sigma^2/2\pi$ as N is white noise.

Next note that from $X(t) = N(t) + N(t-s)$

$$dZ_X(\lambda) = [1 + e^{-i\lambda s}] dZ_N(\lambda)$$

Writing expression (4.5) in the frequency domain

$$d\mathbf{Z}_{\mathbf{S}}(\lambda) = \mathbf{A}_1(\lambda) dZ_X(\lambda) + \int \mathbf{A}_2(\lambda-\beta,\beta) dZ_X(\lambda-\beta) dZ_X(\beta) + \iint \mathbf{A}_3(\lambda-\beta-\gamma,\beta,\gamma) dZ_X(\lambda-\beta-\gamma) dZ_X(\beta) dZ_X(\gamma)$$

Supposing the third cumulant κ_3 of N to be zero, the second term here may be ignored in the computations to come. The last expression is then

$$\mathbf{A}_1(\lambda)[1 + e^{-\lambda s}] dZ_N(\lambda) + \iint \mathbf{A}_3(\lambda-\beta-\gamma,\beta,\gamma)[1 + e^{-is(\lambda-\beta-\gamma)}][1 + e^{-is\beta}][1 + e^{-is\gamma}] dZ_N(\lambda-\beta-\gamma) dZ_N(\beta) dZ_N(\gamma)$$

And so

$$\mathbf{f}_{SN}(\lambda)\delta(0) = E\{dZ_{\mathbf{S}}(\lambda) dZ_N(-\lambda)\} = \mathbf{A}_1(\lambda)[1 + e^{-i\lambda s}]\delta(0)\frac{\sigma^2}{2\pi} +$$
$$\iint \mathbf{A}_3(\lambda-\beta-\gamma,\beta,\gamma)[1 + e^{-is(\lambda-\beta-\gamma)}][1 + e^{-is\beta}][1 + e^{-is\gamma}]\left[\{\delta(\beta+\gamma)^2 + \delta(\lambda-\beta)^2 + \delta(\lambda-\gamma)^2\}\frac{\sigma^4}{(2\pi)^2} + \delta(0)\frac{\kappa_4}{(2\pi)^3}\right] d\beta d\gamma$$

From the assumed symmetry of $\mathbf{A}_3$, this gives (4.8).

Finally, to get expression (4.9) expand $|1 + e^{-i\nu s}|^2$, multiply by $e^{-i\mu s}$, and integrate using $\int e^{-i\mu s} ds = 2\pi\delta(\mu)$.

Figure 1

2,3-dibromothiophene

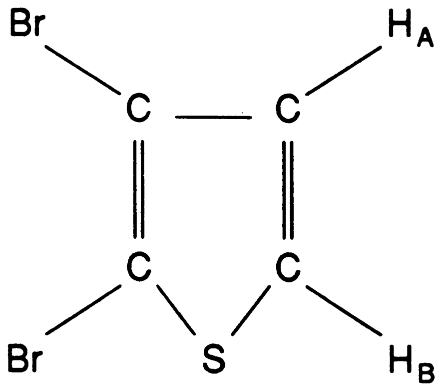

Figure 2

$$\frac{d\rho_{11}}{dt} = \frac{i}{2}\{(\rho_{12}-\rho_{21})(c+s) + (\rho_{13}-\rho_{31})(c-s)\}\gamma x \;-\; (\rho_{11}-\rho_{11}^{T})/T_1$$

$$\frac{d\rho_{22}}{dt} = \frac{i}{2}(\rho_{21}-\rho_{12} + \rho_{24}-\rho_{42})(c+s)\gamma x \;-\; (\rho_{22}-\rho_{22}^{T})/T_1$$

$$\frac{d\rho_{33}}{dt} = \frac{i}{2}(\rho_{31}-\rho_{13} + \rho_{34}-\rho_{43})(c-s)\gamma x \;-\; (\rho_{33}-\rho_{33}^{T})/T_1$$

$$\frac{d\rho_{44}}{dt} = \frac{i}{2}\{(\rho_{42}-\rho_{24})(c+s) + (\rho_{43}-\rho_{34})(c-s)\}\gamma x \;-\; (\rho_{44}-\rho_{44}^{T})/T_1$$

$$\frac{d\rho_{12}}{dt} = \frac{i}{2}\rho_{12}(J-\sqrt{\ }+\omega_A+\omega_B) + \frac{i}{2}\{(\rho_{11}-\rho_{22}+\rho_{14})(c+s)-\rho_{32}(c-s)\}\gamma x \;-\; \rho_{12}/T_{2B}$$

$$\frac{d\rho_{13}}{dt} = \frac{i}{2}\rho_{13}(J+\sqrt{\ }+\omega_A+\omega_B) + \frac{i}{2}\{(\rho_{11}-\rho_{33}+\rho_{14})(c-s)-\rho_{23}(c+s)\}\gamma x \;-\; \rho_{13}/T_{2A}$$

$$\frac{d\rho_{14}}{dt} = i\rho_{14}(\omega_A+\omega_B) + \frac{i}{2}\{(\rho_{12}-\rho_{24})(c+s)+(\rho_{13}-\rho_{34})(c-s)\}\gamma x \;-\; \rho_{14}/T_{2D}$$

$$\frac{d\rho_{23}}{dt} = i\rho_{23}\sqrt{\ } + \frac{i}{2}\{(\rho_{21}+\rho_{24})(c-s) - (\rho_{13}+\rho_{43})(c+s)\}\gamma x \;-\; \rho_{23}/T_{2Z}$$

$$\frac{d\rho_{24}}{dt} = \frac{i}{2}\rho_{24}(-J+\sqrt{\ }+\omega_A+\omega_B) + \frac{i}{2}\{(\rho_{22}-\rho_{44}-\rho_{14})(c+s)+\rho_{23}(c-s)\}\gamma x \;-\; \rho_{24}/T_{2A}$$

$$\frac{d\rho_{34}}{dt} = \frac{i}{2}\rho_{34}(-J-\sqrt{\ }+\omega_A+\omega_B) + \frac{i}{2}\{(\rho_{33}-\rho_{44}-\rho_{14})(c-s)+\rho_{32}(c+s)\}\gamma x \;-\; \rho_{34}/T_{2B}$$

Figure 3

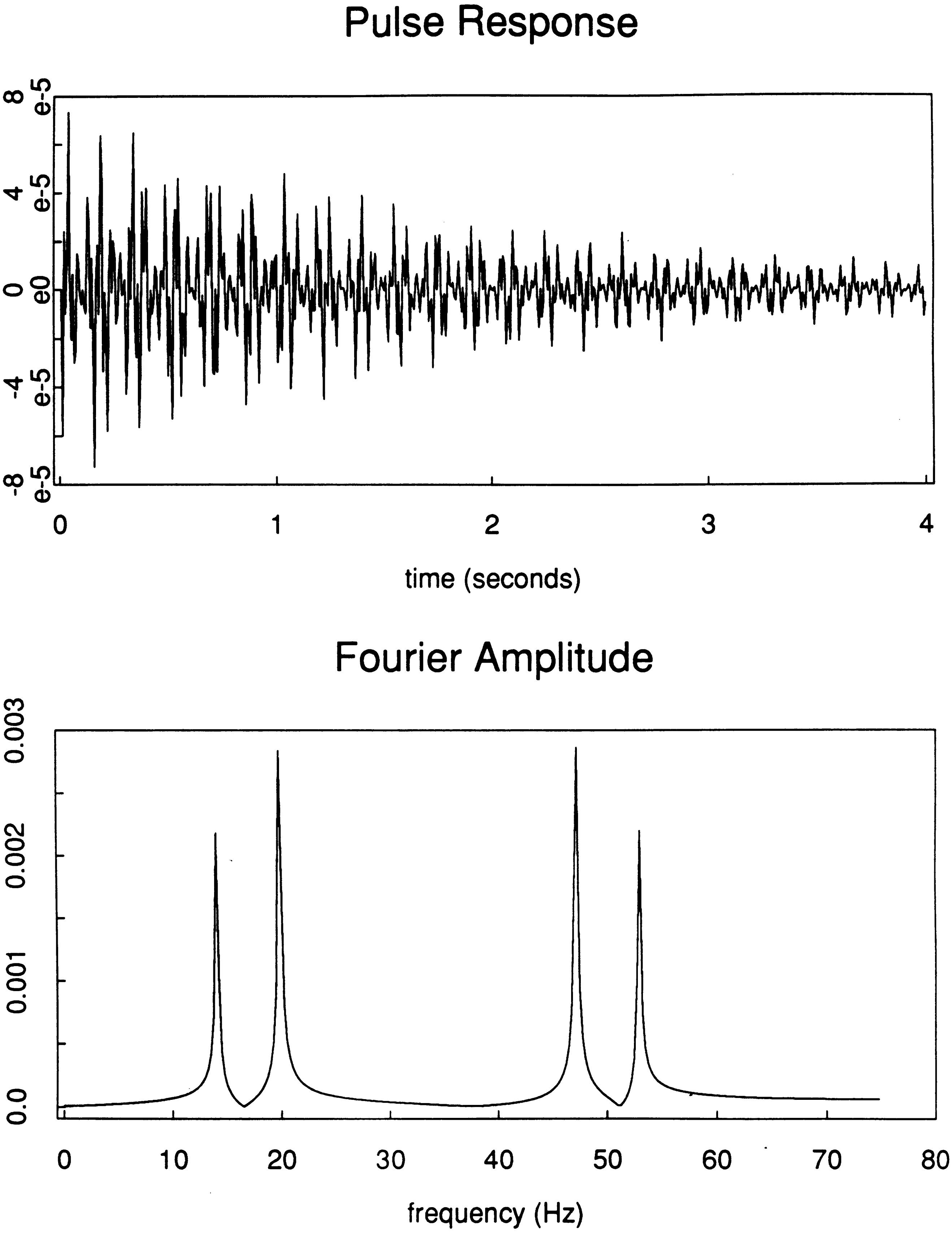

Pulse Response

Fourier Amplitude

Figure 4

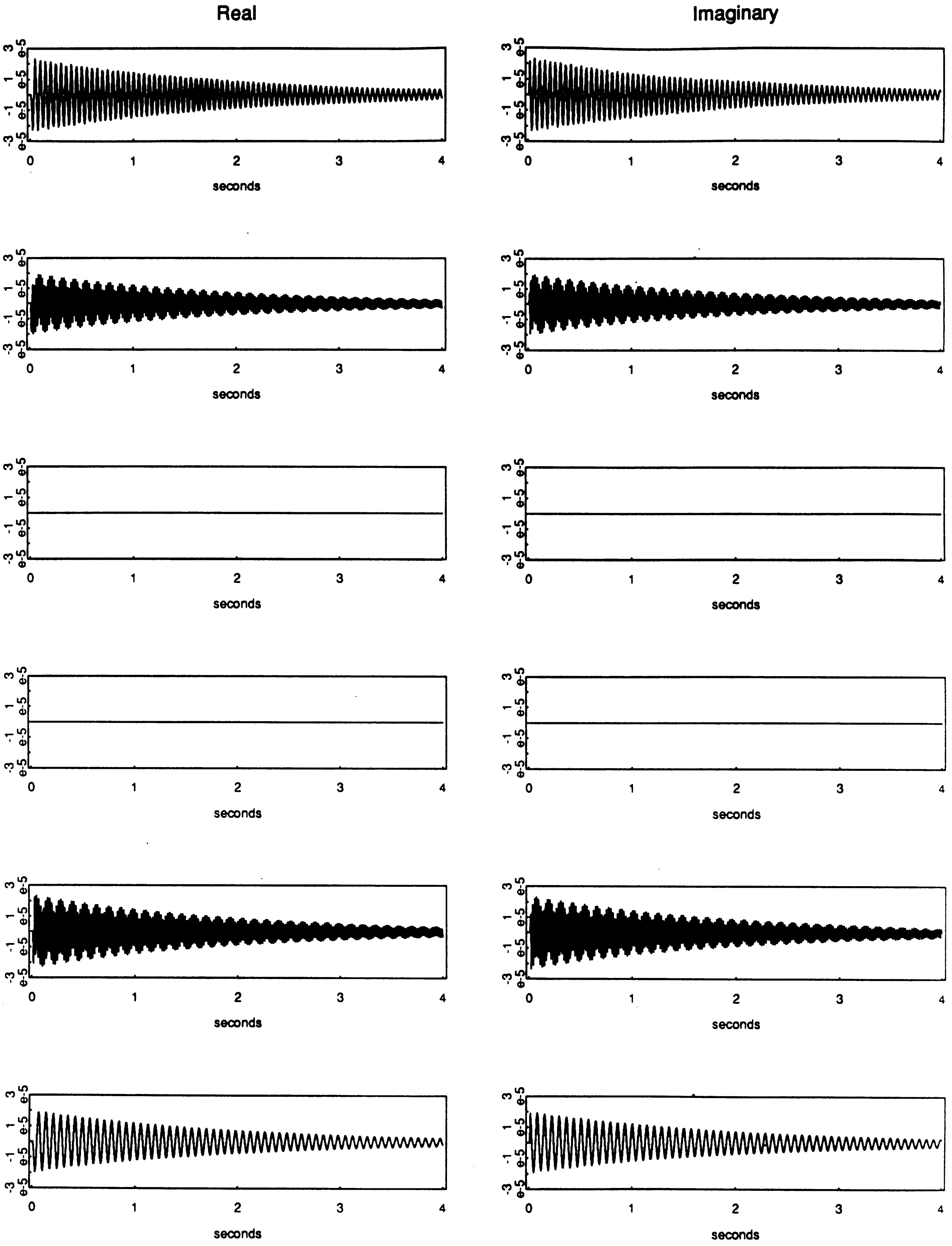

Figure 5

Frequency = 52.94 Hz, sampling rate 150 Hz

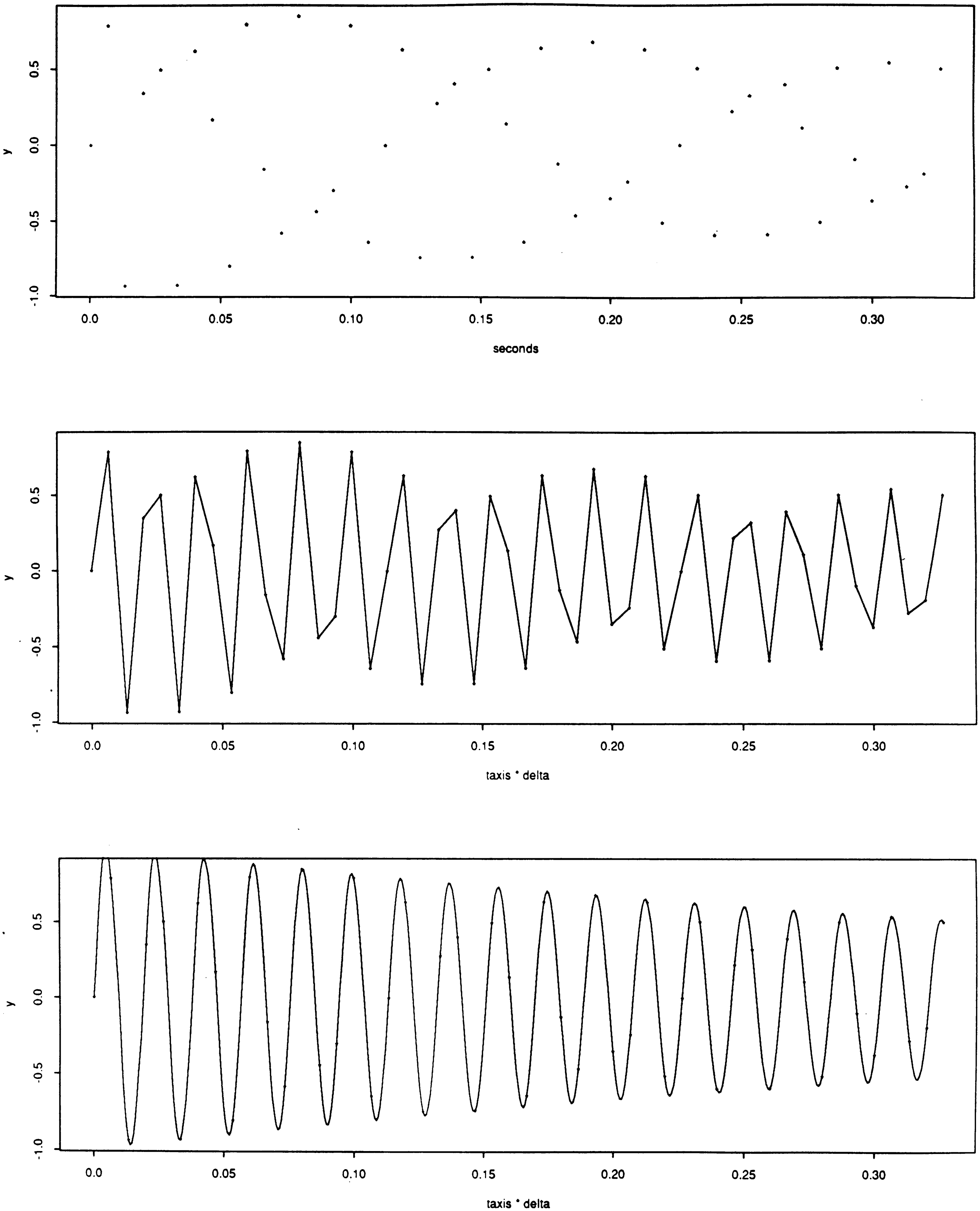

Figure 6

Two-pulse Fourier amplitude - 1 degree flip angle

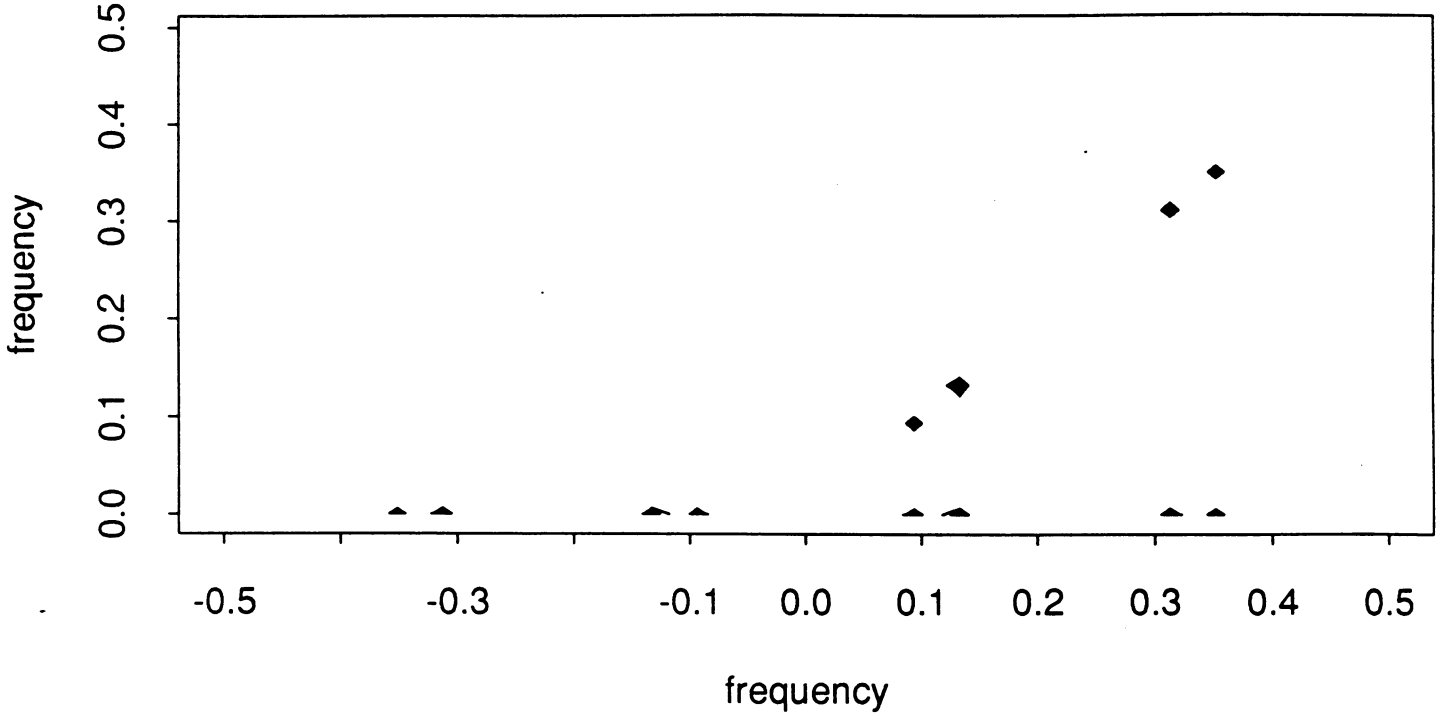

Two-pulse Fourier amplitude - 90 degree flip angle

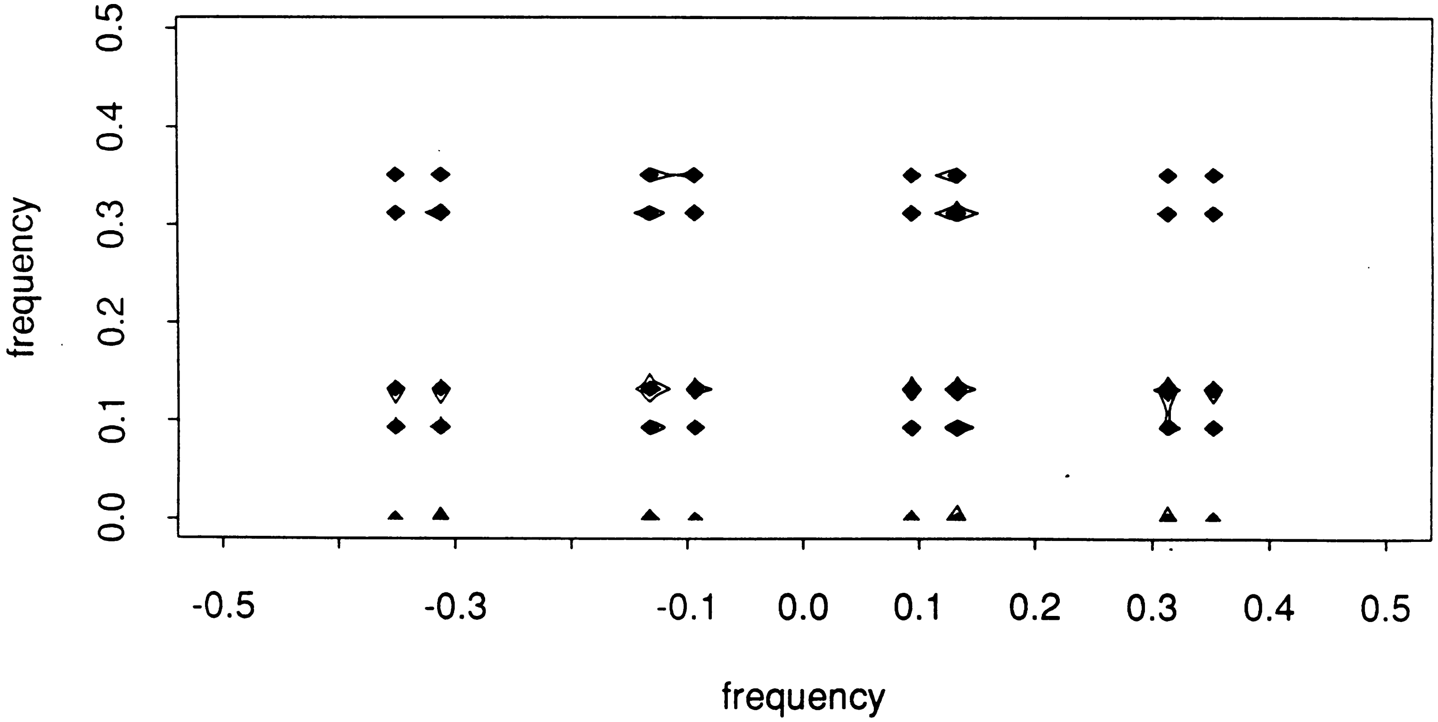

Figure 7

Transfer function amplitude - 10 degree flip angle

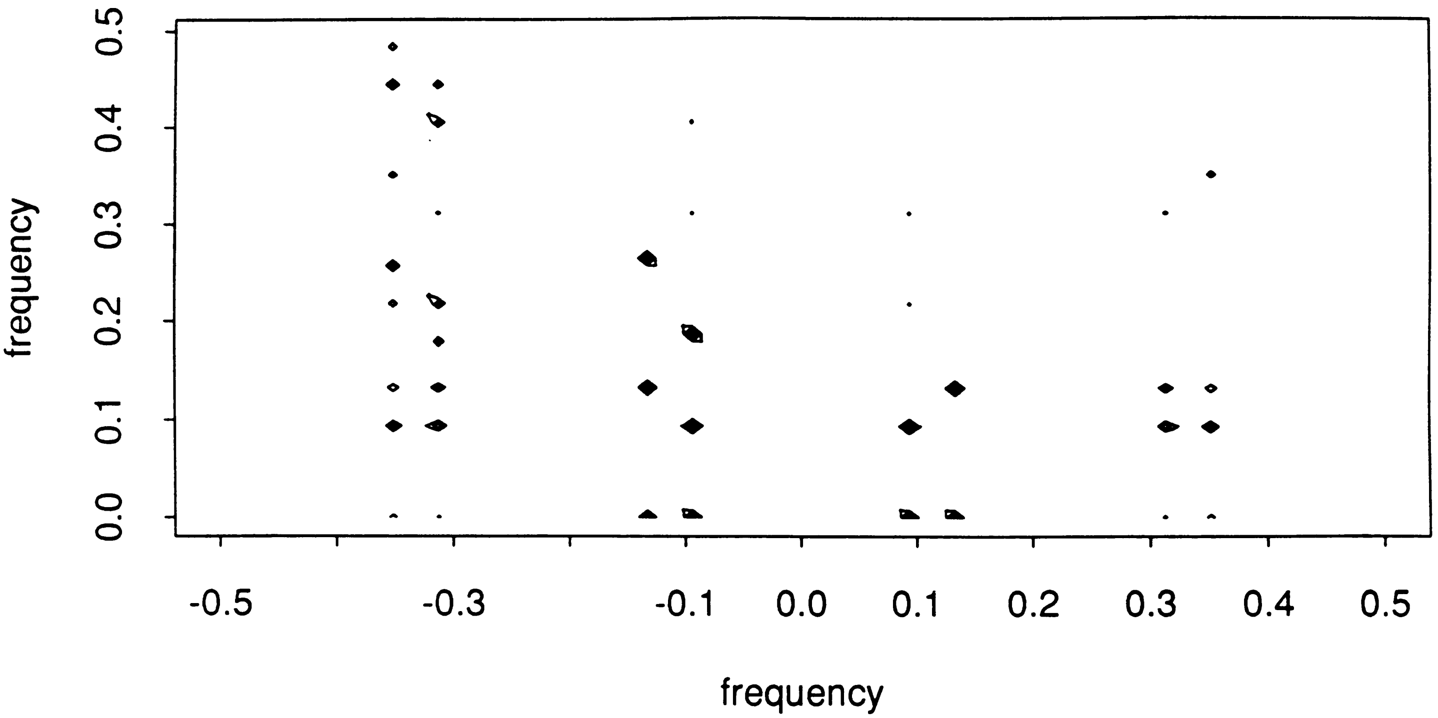

Hybrid analysis Fourier amplitude - 10 degree flip angle

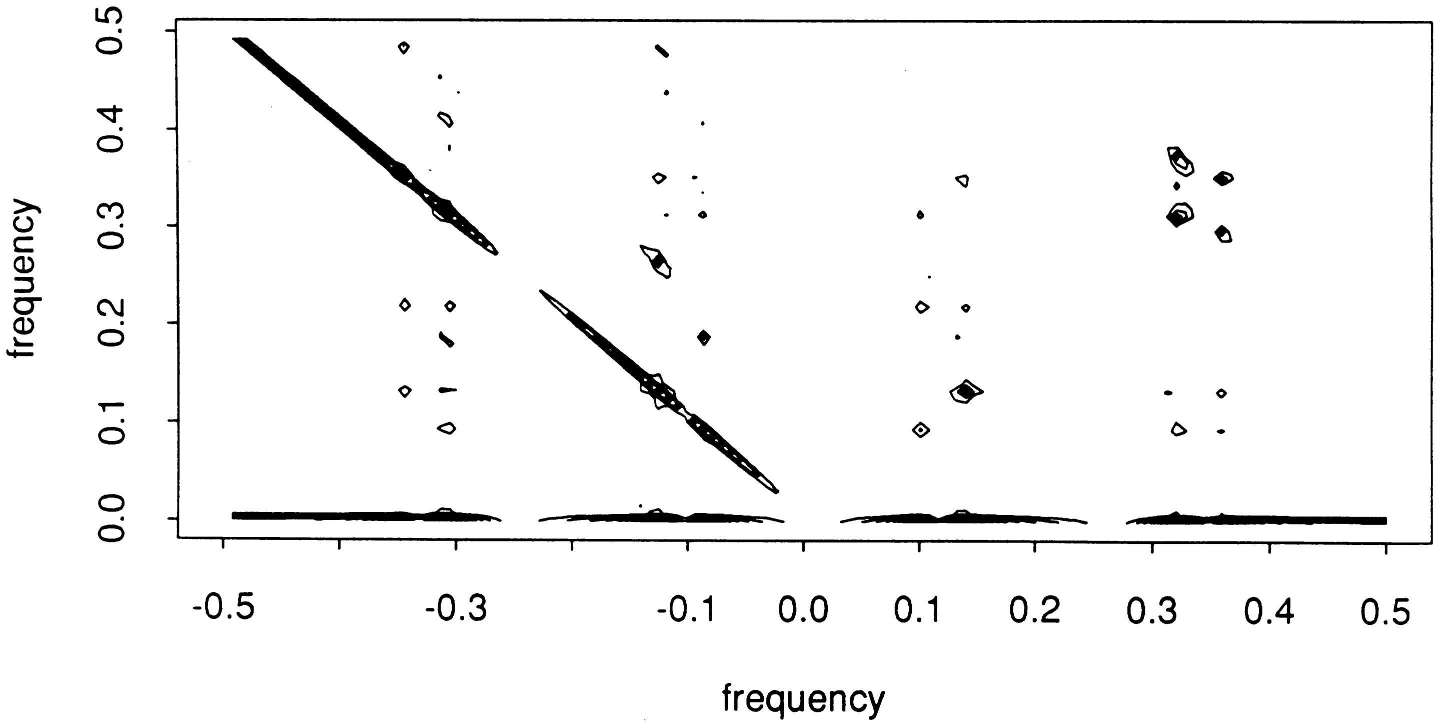

Figure 8

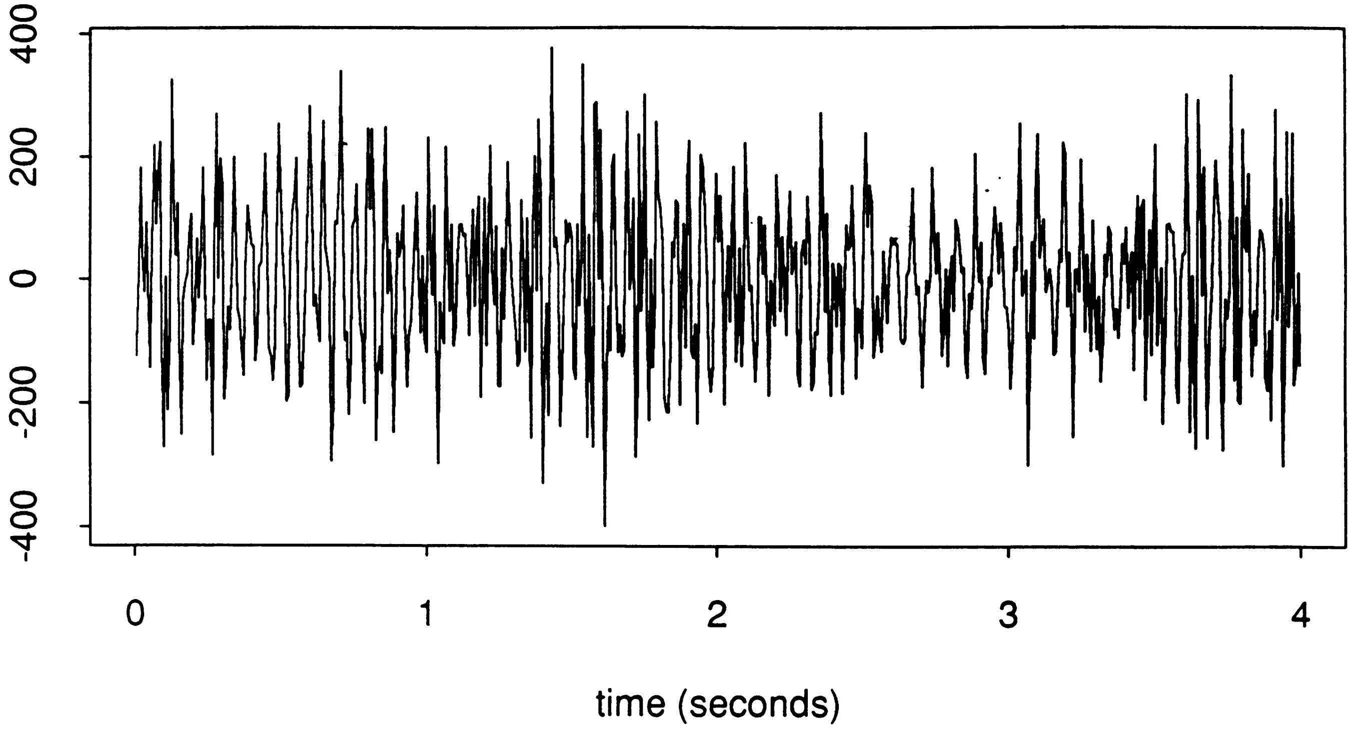
Noise Response

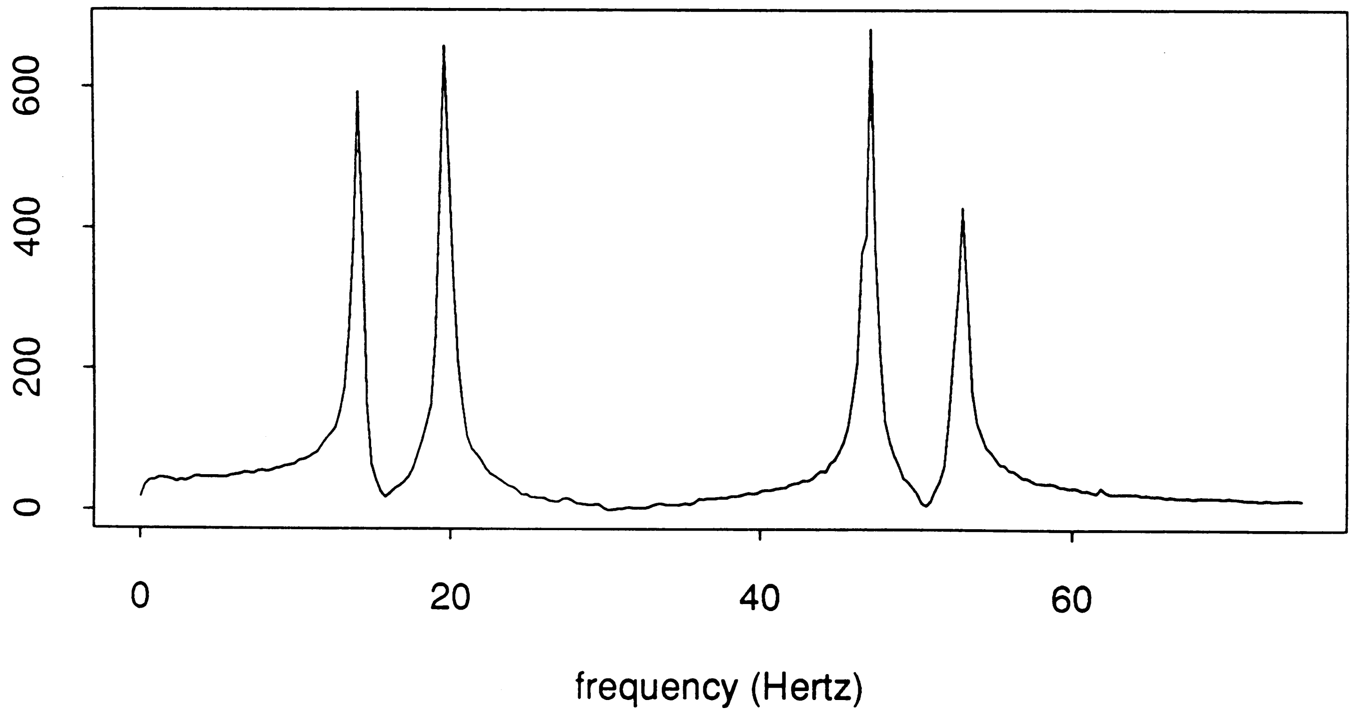
Modulus Transfer Function

Figure 9 - Complete Data Set

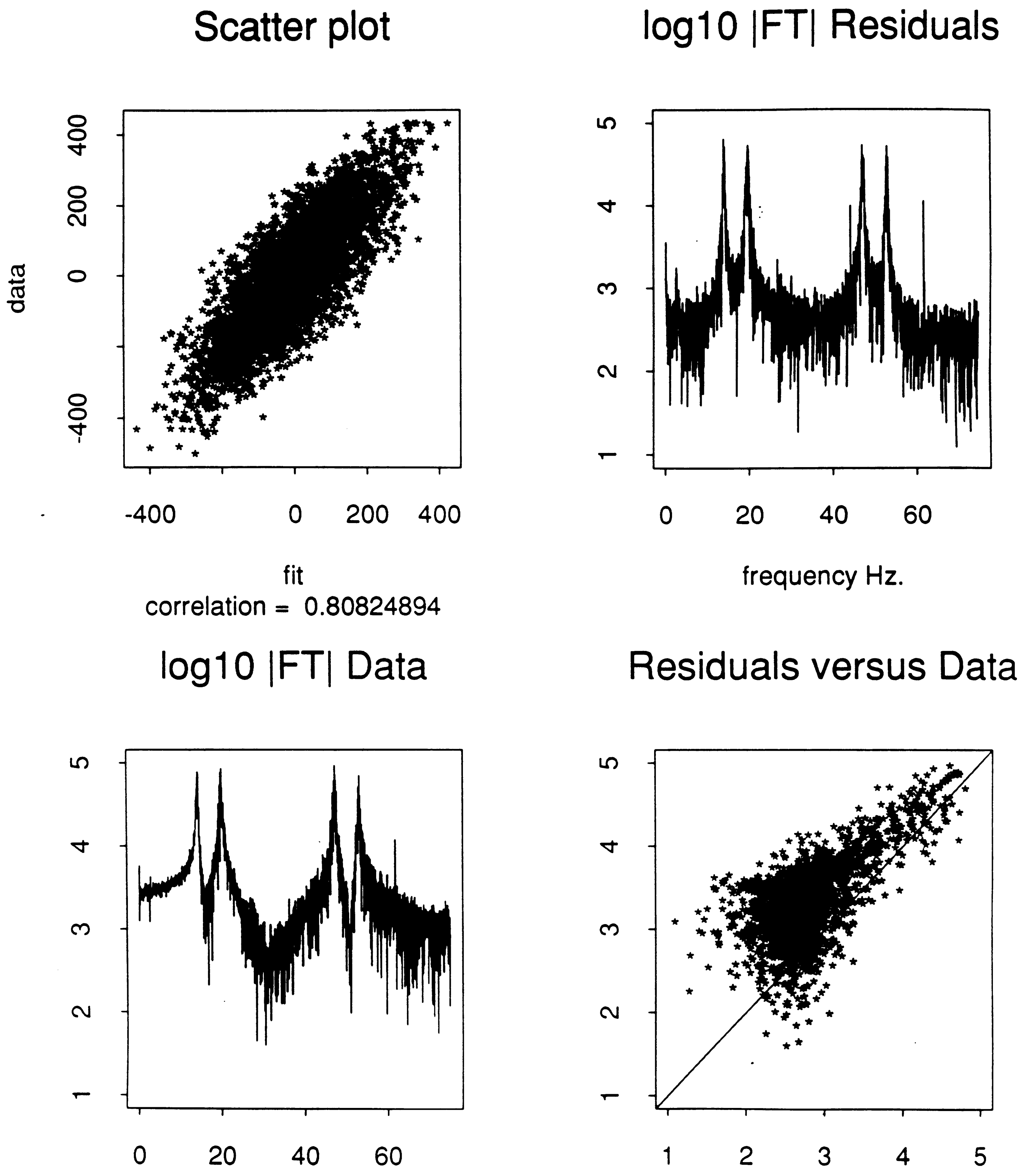

Scatter plot

log10 |FT| Residuals

log10 |FT| Data

Residuals versus Data

correlation = 0.80824894

Figure 10 - First 1000 Points

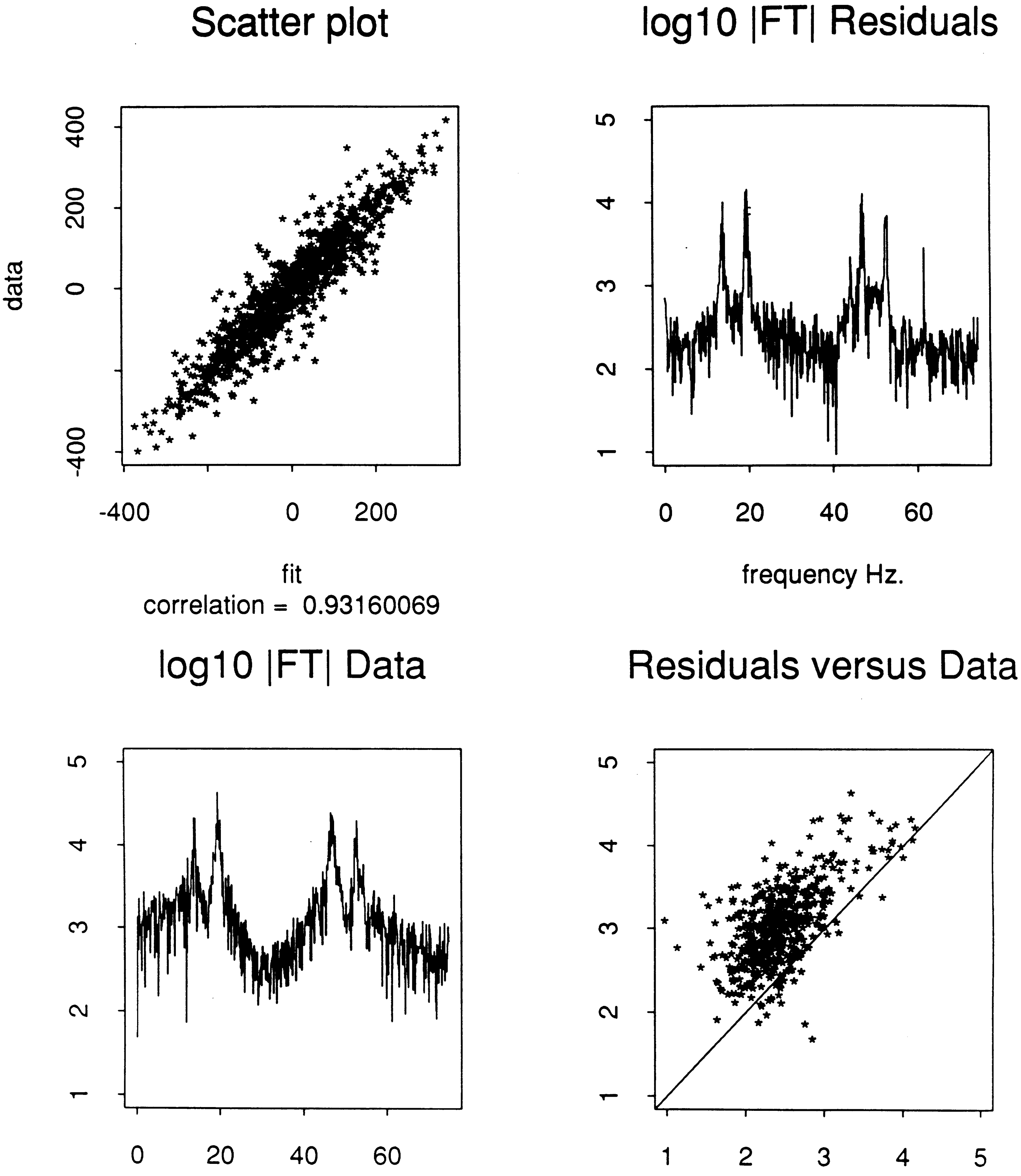

Figure 11 - Second 1000 Points

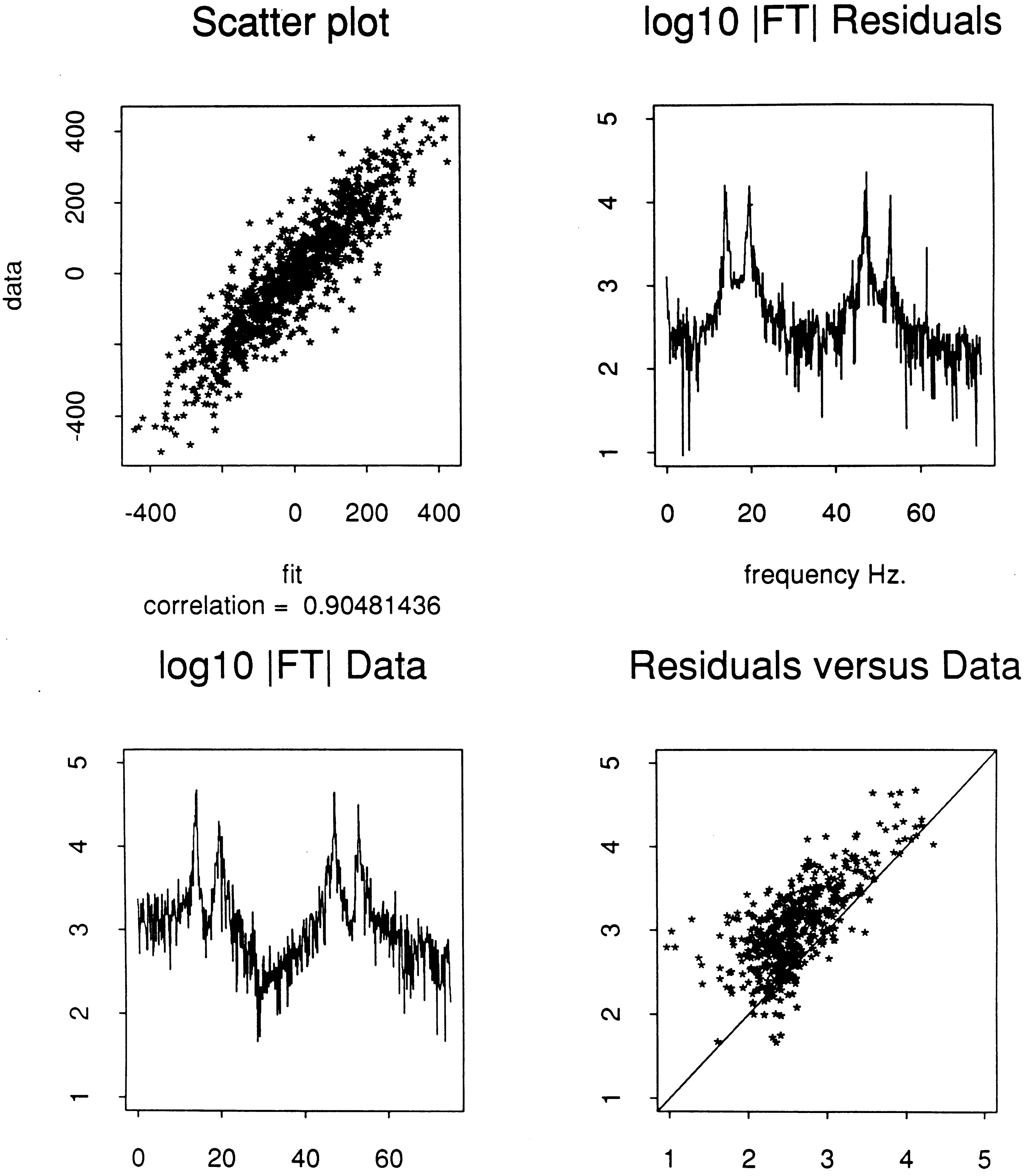

Scatter plot

log10 |FT| Residuals

log10 |FT| Data

Residuals versus Data

correlation = 0.90481436

Figure 12 - Third 1000 Points

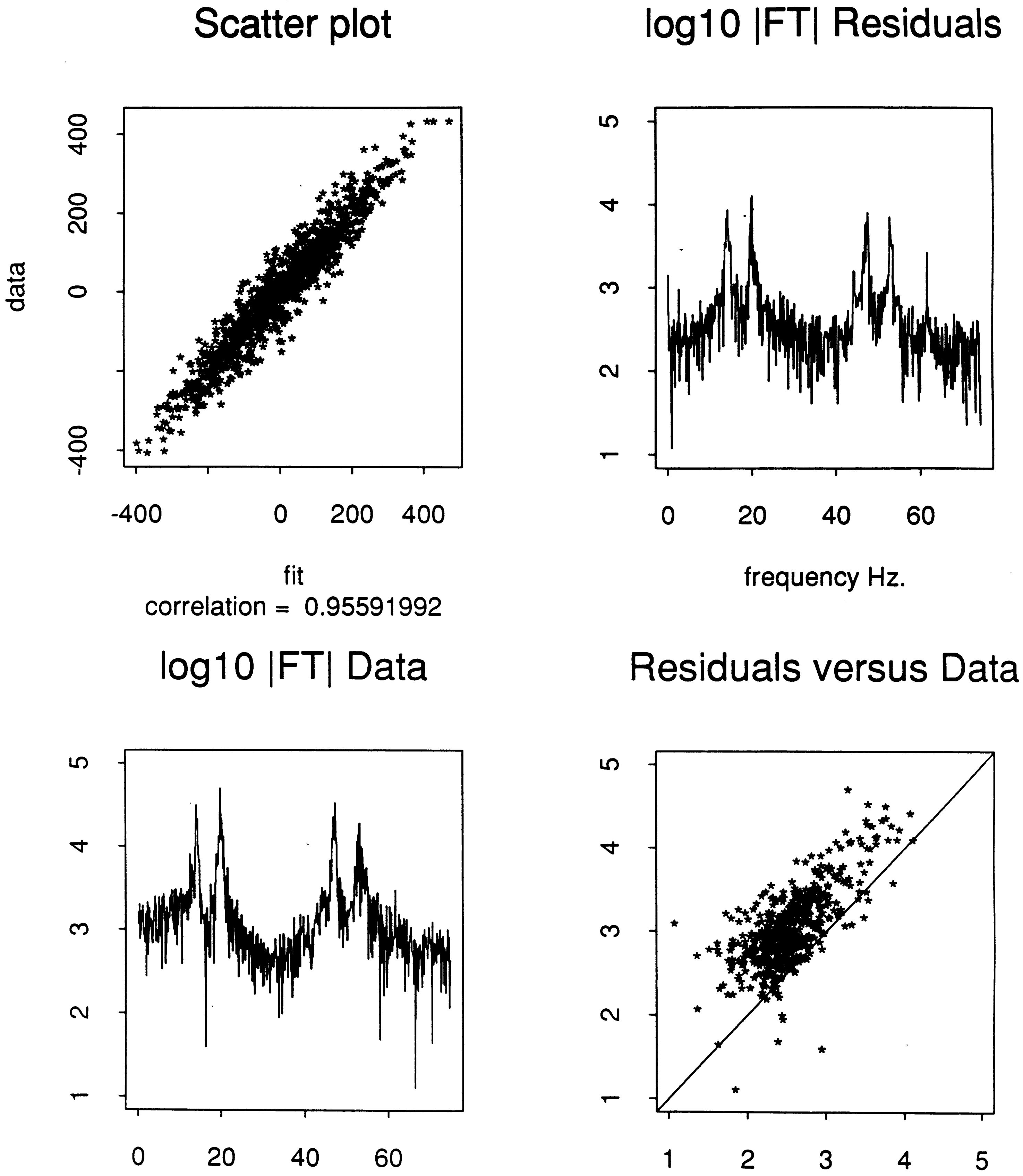

Scatter plot

log10 |FT| Residuals

correlation = 0.95591992

log10 |FT| Data

Residuals versus Data

Figure 13 - Fourth 1000 Points

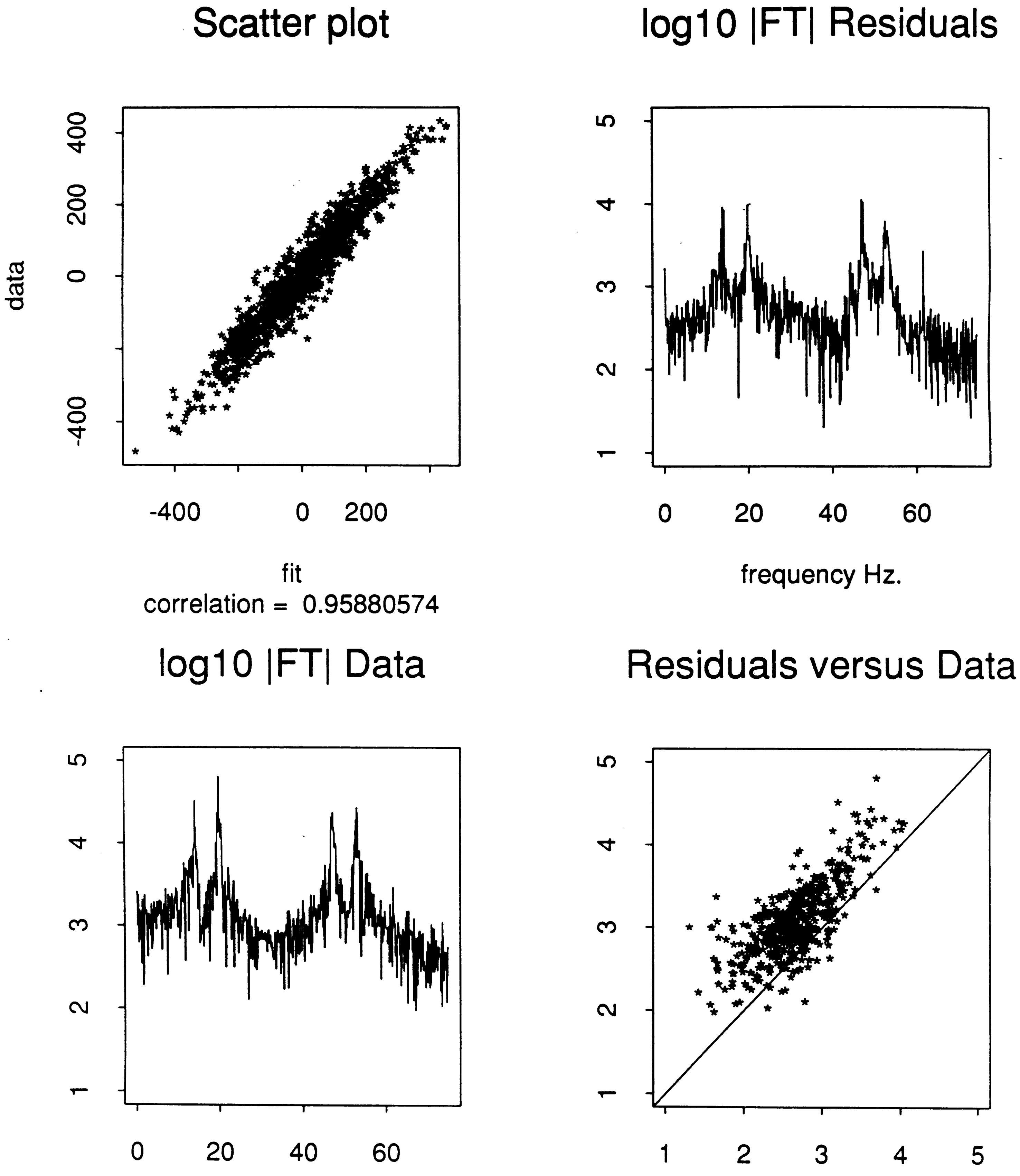

Scatter plot

log10 |FT| Residuals

log10 |FT| Data

Residuals versus Data